Non-uniform TFA reduced multiscale procedure for shell-3D modeling of periodic masonry structures

Daniela Addessi[a], Paolo Di Re[a,*], Cristina Gatta[a], Elio Sacco[b]

[a]*Department of Structural and Geotechnical Engineering, Sapienza University of Rome, Via Eudossiana 18, 00184 Rome, Italy,*
{daniela.addessi, paolo.dire, cristina.gatta}@uniroma1.it
[b]*Department of Structures for Engineering and Architecture, University of Naples Federico II, Via Claudio 21, 80125 Naples, Italy,*
elio.sacco@unina.it

Abstract

This work proposes a reduced-order multiscale model for the analysis of masonry elements subjected to in-plane and out-of-plane loading conditions. The Transformation Field Analysis (TFA) is adopted to link the homogeneous shell model at the macroscale with a three-dimensional (3D) representative unit cell (UC) of the masonry material defined at the microscale, accounting for the regular arrangement of bricks/blocks and mortar joints. The UC is modeled considering linear elastic bricks joined by interfaces subjected to possible damage and frictional plasticity mechanisms. An enhanced TFA procedure is proposed, discretizing the interfaces in subsets where non-uniform distribution of the inelastic quantities is considered and the plastic-damage evolution problem solved. Numerical simulations are developed to assess the advantages and drawbacks of the non-uniform TFA approach compared to previously proposed piece-wise uniform procedure. The results obtained through the proposed numerical approach are compared with both micromechanical and experimental outcomes.

Keywords: Masonry, Out-of-plane mechanims, Nonlinear interfaces, Multiscale, Non-uniform TFA

1. Introduction

Masonry structures are a relevant part of the cultural and architectural heritage of many European countries. They are often vulnerable constructions as they are old buildings, sometime deteriorated because of the lack of due maintenance. Moreover, the masonry material is often characterized by poor mechanical properties, making the constructions significantly exposed to damage risk.

Several methods and procedures are available in literature to reproduce and analyze the response of masonry constructions, aimed at assessing their safety conditions and determining their maximum load and displacement capacities. A quite extensive review is reported, for instance, in [5, 11, 20, 21, 30], describing the most adopted approaches available to evaluate the behavior of both reinforced and unreinforced masonry structures. These can be classified as follows:

---

*Corresponding author:
E-mail address: paolo.dire@uniroma1.it (P. Di Re)

- Damage, Plasticity and Fracture models within Finite Element (FE), Discrete Element or Finite Difference numerical methods [9, 10, 19, 26, 27, 31];

- Limit Analysis approaches [6, 14, 18, 24, 25], with their kinematic or static formulations, as the Thrust Network Analysis;

- Homogenization and Multiscale techniques [2, 15, 26, 27].

The multiscale approach represents a challenging opportunity for determining the mechanical response of masonry constructions, viable at the structural scale, but satisfactorily accurate at the microscale. With the aim of optimizing the reliability of the procedure with respect to the computational burden, a reduced-order multiscale model is proposed in [4] for the analysis of masonry walls subjected to in-plane loading conditions, showing the considerable computational advantages compared to more classical FE^2 multiscale techniques [22, 29, 34]. A uniform Transformation Field Analysis (TFA) is adopted in [4] to solve the nonlinear homogenization problem and, hence, to link the homogeneous two-dimensional (2D) continuum model adopted at the macroscale with a 2D representative unit cell (UC) of the masonry material properly defined at the microscale, accounting for the regular arrangement of bricks/blocks and mortar joints. Relying on the assumption that the material nonlinear mechanims only occur in the mortar joints, the key idea is to discretize the whole domain composed by the mortar joints included in the UC into regions, called *subsets*, where uniform distributions of the inelastic quantities are considered. Hence, the nonlinear constitutive response of the macroscopic masonry material is directly computed from the average values of the inelastic strains of each subset.

A similar approach is adopted in [2] for the analysis of masonry elements under both in-plane and out-of-plane loading conditions. Indeed, a new shell-3D model is there proposed, where a shell element at the macroscale is linked to a 3D solid model of the UC at the microscale. Linear elastic response is considered for the bricks, while all nonlinearities are assumed to arise in the mortar joints. This model is then applied in [3] for the analysis of curved masonry elements, such as vaults and domes.

The studies developed in [2, 3] show that the piece-wise uniform distribution assumed for the mortar joint inelastic strains, within the shell-3D multiscale model under plate bending and torsional strain states, requires a fine subset subdivision of the UC to obtain an accurate representation of the masonry response, hence leading to computationally demanding structural models. Indeed, extensive numerical analyses are conducted in [3] to investigate the influence of the subset discretization in terms of solution accuracy and required computational effort.

In the present work, a Non-Uniform TFA (NUTFA) approach, inspired to the procedure proposed in [33], is developed. Linear (instead of uniform) distribution of the inelastic strain field within each subset is assumed. Thus, the macroscopic masonry constitutive behavior is determined from the corresponding average values and additional parameters associated to the higher order contributions. Specifically, based on the results in [2, 3], the proposed approach considers a linear profile along the UC in-plane axes of the inelastic strain components directed along the

UC thickness. The optimal linear profile is determined through a least square minimization defined with respect to the strains occurring at selected points of each subset.

Of course, the introduction of new parameters ruling the linear profile of the inelastic quantities leads to an increase of the computational complexity. Hence, a comprehensive comparison is presented in terms of advantages and disadvantages of adopting the uniform TFA or NUTFA scheme and suitable criteria to select the proper subset layout are given, to obtain a fair compromise between accuracy and computational effort of the model. To this end, numerical applications are performed on a single UC to study the improvements introduced by NUTFA under bending and torsional deformations. Moreover, the response of real scale masonry elements is investigated and the results obtained through the proposed model are compared with experimental and micromechanical outcomes.

2. Macroscale description

At the macroscale, the proposed model considers a flat shell formulation based on the Mindlin-Reissner theory, i.e. including the contribution of the shear deformations. The shell formulation is defined in the local reference system (X_1, X_2, X_3), being X_1 and X_2 the directions that lie in the mid-plane of the element and X_3 that running across the shell thickness (Fig. 1).

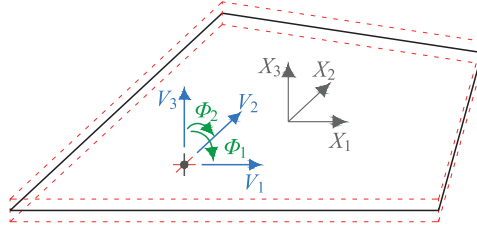Figure 1: Schematic of the shell model at the macroscale

The element kinematics is described by introducing the shell generalized displacement fields, i.e. the mid-plane translation displacements $V_1(X_1, X_2)$, $V_2(X_1, X_2)$ and $V_3(X_1, X_2)$ and the shell orthogonal fiber rotations $\Phi_1(X_1, X_2)$ and $\Phi_2(X_1, X_2)$ about the directions X_2 and $-X_1$, respectively. These are collected in the vector $\mathbf{V}(X_1, X_2)$.

The eight generalized shell strains, i.e. the membrane strains $E_{11}(X_1, X_2)$, $E_{22}(X_1, X_2)$ and $\Gamma_{12}(X_1, X_2)$, the plate curvatures $K_{11}(X_1, X_2)$, $K_{22}(X_1, X_2)$ and $K_{12}(X_1, X_2)$ and the plate shear strains $\Gamma_{13}(X_1, X_2)$ and $\Gamma_{23}(X_1, X_2)$ are collected in the vector $\mathbf{E}(X_1, X_2)$, i.e.:

$$\mathbf{E} = \left\{ E_{11} \quad E_{22} \quad \Gamma_{12} \quad K_{11} \quad K_{22} \quad K_{12} \quad \Gamma_{13} \quad \Gamma_{23} \right\}^T \tag{1}$$

and are related to the shell generalized displacement fields by the standard compatibility conditions [7, 36].

The generalized shell stresses work-conjugate to $\mathbf{E}(X_1, X_2)$ are the membrane, bending and shear resultants, collected in the vector $\mathbf{\Sigma}(X_1, X_2)$, i.e.:

$$\mathbf{\Sigma} = \left\{ N_{11} \quad N_{22} \quad N_{12} \quad M_{11} \quad M_{22} \quad M_{12} \quad Q_{13} \quad Q_{23} \right\}^T \tag{2}$$

3

The constitutive relationship between generalized shell strains $\mathbf{E}(X_1, X_2)$ and stresses $\mathbf{\Sigma}(X_1, X_2)$ is obtained from the analysis of the UC defined at the microscale and the adoption of a proper homogenization procedure, as described in the following.

The presented flat shell element can be successfully adopted to reproduce the response of plane structures, such as masonry walls. To study the behavior of vaults and domes, the proposed model must be formulated in a three-dimensional space, making use of appropriate rotation matrices, and introducing the additional kinematic parameter of the drilling rotation, in order to join non-coplanar elements [3].

3. Microscale description

At the microscale, the proposed model describes masonry material with periodic texture as a heterogeneous 3D Cauchy continuum. Thus, a periodic UC is defined and referred to for the computational homogenization. Within the UC, the bricks defining the sub-domain Ω_b are assumed to exhibit a linear elastic response, while the mortar joints defining the sub-domains $\mathfrak{I}_b$ (bed) and $\mathfrak{I}_h$ (head) are characterized by a cohesive-frictional mechanical response and are modeled with zero-thickness plane interfaces.

Fig. 2(a) shows an example of UC for a running bond texture with single leaf, where Ω_b, $\mathfrak{I}_b$ and $\mathfrak{I}_h$ are distinguished with different colors. The reference system (x_1, x_2, x_3) is assumed, being x_1 and x_2 the directions that lie in the mid-plane of the UC and x_3 that running across the thickness. The dimensions of the UC along x_1, x_2 and x_3 are indicated with $2\,a_1$, $2\,a_2$ and t, respectively.

(a)
(b)
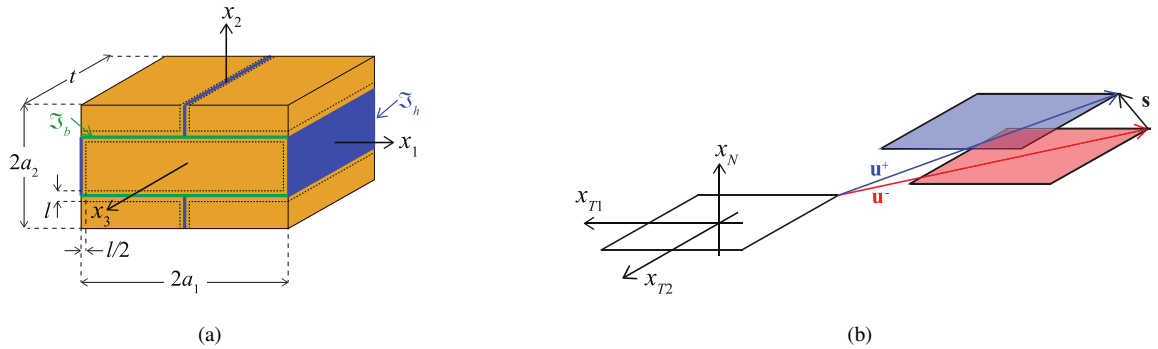
Figure 2: Example of (a) the UC considered at microscale and (b) schematic of the interface model adopted for the mortar joints

In the UC, the displacement fields, $\mathbf{u} = \{u_1 \; u_2 \; u_3\}^T$, are defined as the sum of two contributions: $\bar{\mathbf{u}}(x_1, x_2, x_3)$ representing the known contribution, obtained from the macroscopic shell strains $\mathbf{E}(x_1, x_2)$, and $\mathbf{u}^\star(x_1, x_2, x_3)$ representing the unknown perturbation due to the material heterogeneity.

Due to the presence of the interfaces, $\mathbf{u}^\star(x_1, x_2, x_3)$ is discontinuous in the UC [35] and must satisfy the periodic conditions imposed at the boundaries. Accordingly, in the bricks, where $\mathbf{u}^\star(x_1, x_2, x_3)$ is continuous, the material strains are obtained from the compatibility conditions with the displacements, defined under linear geometry assump-

4

tion, and result as:

$$\boldsymbol{\varepsilon}^b = \mathbf{B}\,\mathbf{E} + \boldsymbol{\varepsilon}^{b\star} \tag{3}$$

where $\boldsymbol{\varepsilon}^b = \left\{\varepsilon_{11}^b\ \varepsilon_{22}^b\ \varepsilon_{33}^b\ \gamma_{12}^b\ \gamma_{13}^b\ \gamma_{23}^b\right\}^T$ and $\boldsymbol{\varepsilon}^{b\star} = \left\{\varepsilon_{11}^{b\star}\ \varepsilon_{22}^{b\star}\ \varepsilon_{33}^{b\star}\ \gamma_{12}^{b\star}\ \gamma_{13}^{b\star}\ \gamma_{23}^{b\star}\right\}^T$ are the total and perturbation strain vectors, respectively, while $\mathbf{B}(x_3)$ is the matrix ruling the strain map transition from the macroscale to the microscale [2], i.e.:

$$\mathbf{B} = \begin{bmatrix} 1 & 0 & 0 & x_3 & 0 & 0 & 0 & 0 \\ 0 & 1 & 0 & 0 & x_3 & 0 & 0 & 0 \\ 0 & 0 & 0 & 0 & 0 & 0 & 0 & 0 \\ 0 & 0 & 1 & 0 & 0 & x_3 & 0 & 0 \\ 0 & 0 & 0 & 0 & 0 & 0 & 1 & 0 \\ 0 & 0 & 0 & 0 & 0 & 0 & 0 & 1 \end{bmatrix} \tag{4}$$

The stresses in the bricks result from the linear elastic constitutive relationship $\boldsymbol{\sigma}^b = \mathbf{C}^b\boldsymbol{\varepsilon}^b$, being $\mathbf{C}^b(x_1, x_2, x_3)$ the material elastic stiffness matrix.

To be noted is that, while the UC local axis x_3 always coincides with the macroscopic shell direction X_3, axes x_1 and x_2 may be rotated with respect to the corresponding macroscopic shell directions X_1 and X_2. Hence, before applying Eq. (3), proper rotation may be required to express the components of $\mathbf{E}$ from the macroscopic shell to the microscopic UC reference system. The details of this transformation are reported in [3].

As for the interface elements, as shown in the example of Fig. 2(a), those composing $\mathfrak{I}_b$ lie in planes parallel to x_1-x_3, while those composing $\mathfrak{I}_h$ lie in planes parallel to x_2-x_3. Hence, to consider a unique description of the interface constitutive response, a local reference system (x_{T1}, x_{T2}, x_N) is introduced for the general element, as depicted in Fig. 2(b). Accordingly, the difference of the displacements $\mathbf{u}^+(x_{T1}, x_{T2}, x_N)$ and $\mathbf{u}^-(x_{T1}, x_{T2}, x_N)$ of the two interface overlapping faces defines the displacement jump $\mathbf{s} = \mathbf{u}^+ - \mathbf{u}^- = \{s_{T1}\ s_{T2}\ s_N\}^T$, being s_{T1}, s_{T2} and s_N the displacement jump components expressed in the interface local reference system.

Denoting by $\mathbf{t} = \{t_{T1}\ t_{T2}\ t_N\}^T$ the interface traction vector, the damage-friction nonlinear model proposed in [4] rules the relationship between $\mathbf{t}(x_{T1}, x_{T2}, x_N)$ and work-conjugate displacement jumps $\mathbf{s}(x_{T1}, x_{T2}, x_N)$. This is expressed as:

$$\mathbf{t} = \mathbf{C}\,(\mathbf{s} - \boldsymbol{\pi}) \tag{5}$$

where $\mathbf{C} = \text{diag}\,\{C_T, C_T, C_N\}$ is the diagonal elastic stiffness matrix of the interface constitutive relationship, being C_T and C_N the stiffness values in the tangential and normal direction to the interface plane, respectively. Vector $\boldsymbol{\pi} = \{\pi_{T1}\ \pi_{T2}\ \pi_N\}^T$ indicates the inelastic displacement jumps and is defined as:

$$\boldsymbol{\pi} = D(\mathbf{c} + \mathbf{p}) \tag{6}$$

5

137 where $\mathbf{c} = \{0 \ 0 \ \langle s_N \rangle_+\}^T$ represents the unilateral contact effect, being $\langle s_N \rangle_+$ the positive part of $s_N(x_{T1}, x_{T2}, x_N)$, and

138 $\mathbf{p} = \{p_{T1} \ p_{T2} \ 0\}^T$ is the sliding frictional relative displacement vector. These latter evolve according to the classical

139 Coulomb yield criterion, on the basis of the friction coefficient μ.

140 Quantity D in Eq. (5) is the damage variable, which accounts for degrading processes caused by sliding and frac-

141 ture opening. Its evolutionary law is ruled by an associated variable defined as function of the normal and tangential

142 displacement jumps, and depends on the mode I and II stress thresholds, t_N^0, t_T^0, and fracture energies, G_{cN} and G_{cT}

143 [2, 3, 4].

144 Perturbation displacements $\mathbf{u}^\star$ and, thus, brick strains and stresses and interface displacement jumps and tractions

145 are determined according to the homogenization procedure described in the following section.

4. Uniform and Non-Uniform TFA-based homogenization procedure

147 The TFA is an effective technique to determine the homogenized response of composite materials [16, 17, 23],

148 successfully applied to masonry. The procedure typically relies on the definition of regions, called *subsets*, where

149 the nonlinear phenomena occur, and the assumption of a prescribed variation for the related nonlinear effects within

150 each subset. In the proposed model, as bricks are considered as linear elastic, the subset subdivision concerns only

151 the interface elements modeling the mortar joints, i.e. $\mathfrak{I}_b$ and $\mathfrak{I}_h$. In this spirit, the response of the masonry UC

152 is determined by superimposing the effects of two terms: the average strains $\mathbf{E}$ in the whole UC and the inelastic

153 displacement jumps $\boldsymbol{\pi}^i$ in each subset $\mathscr{S}^i$ with $(i = 1, ..., n_s)$.

154 In previous studies [2, 3], piece-wise uniform distributions of the nonlinear quantities over mortar joints were

155 assumed, i.e. a uniform TFA approach was adopted, which required fine subset partitions under bending and torsional

156 responses. To avoid such computationally expensive refined partitions, a modified procedure is proposed in this work.

157 It is based on the definition of non-uniform distribution of the inelastic quantities in each subset, i.e. NUTFA approach.

158 Hence, the inelastic strain field in the typical subset $\mathscr{S}^i$ is represented in the following form:

$$\boldsymbol{\pi}^i = \boldsymbol{\pi}_0^i + x_s^i \boldsymbol{\pi}_1^i \tag{7}$$

160 where $\boldsymbol{\pi}_0^i$ denotes the average inelastic displacement jump and the second term represents their linear variation along

161 the in-plane direction x_s^i of the subset. Figure 3(a) shows a possible identification of x_s^i for some subsets of a running

162 bond UC. Here, 2 and 1 subdivisions are considered for bed and head joints, respectively, in the direction parallel

163 to the UC mid-plane, i.e $n_b = 2$ and $n_h = 1$, and, 3 layers are assumed along the UC thickness, i.e $n_t = 3$, so that

164 $n_s = n_t \times (n_h + n_b) = 9$. Without loss of generality, in the following, it is assumed that local direction x_{T2} coincides

165 with the UC thickness direction x_3 for all interface elements and, thus, for all subsets, while x_{T1} and x_N are parallel to

166 the UC plane. In particular, the in-plane direction x_s^i has origin in the middle of the subset and is parallel to x_1 in the

167 bed joints and x_2 in the head joints.

168 Based on the results observed in [2, 3] Eq. (7) is defined to enrich the description of the inelastic displacement

169 jump π_{T2} parallel to the UC thickness. Hence, $\boldsymbol{\pi}_1^i$ has all zero terms except that directed along t, as opposed to $\boldsymbol{\pi}_0^i$

6

that includes all three displacement jump components, i.e. $\boldsymbol{\pi}_0^i = \{\pi_{0,T1}^i \ \pi_{0,T2}^i \ \pi_{0,N}^i\}^T$ and $\boldsymbol{\pi}_1^i = \{0 \ \pi_{1,T2}^i \ 0\}^T$. Figure 3(b) shows the linear variation assumed for π_{T2} in the subdomains of a layer extracted from the UC. In the following, the main two phases of the methodology are described. The first is a pre-processing phase, called 'offline', aimed at evaluating proper localization operators. The last, named 'online' phase, solves the nonlinear evolution problem of the UC by employing information derived from the previous offline computations.

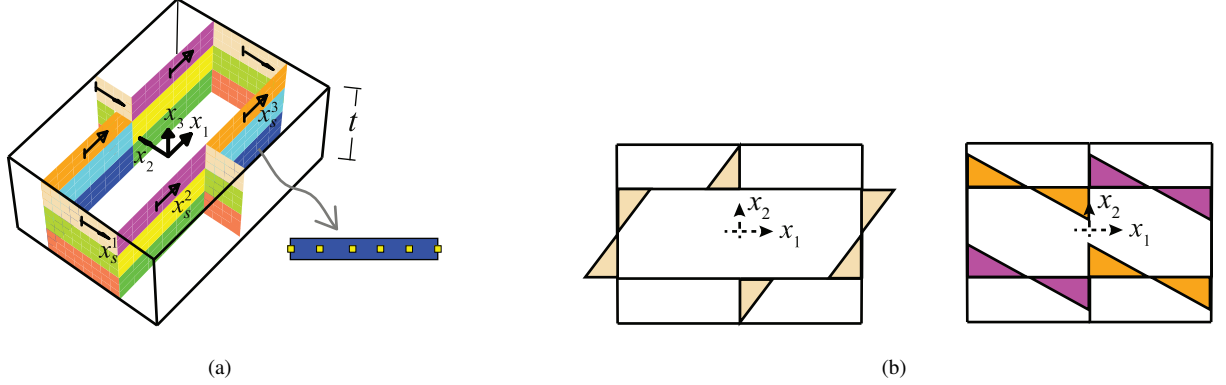(a)   (b)

Figure 3: Running bond UC: (a) possible subset subdivision with $n_t = 3$, $n_h = 1$ and $n_b = 2$; (b) linear variation $x_s^i \pi_{1,T2}^i$ of the inelastic component π_{T2} in the proposed NUTFA (the regions of the interfaces depicted with the same color belong to the same subset)

The procedure to determine $\boldsymbol{\pi}_0^i$ and $\boldsymbol{\pi}_1^i$ is described in the following, where it has to be noted that the uniform TFA approach adopted in [2, 3] is obtained as special case of the NUTFA here proposed by neglecting the linear term in Eq. (7), that is the contribution $x_s^i \boldsymbol{\pi}_1^i$.

4.1. Offline phase

Before performing the nonlinear analysis of the structure, a pre-processing phase is required to evaluate the effects of the macroscopic strains and inelastic displacements jumps on the UC response. Hence, micromechanical linear elastic analyses are performed by prescribing one-by-one a unit value of the components of $\mathbf{E}$, $\boldsymbol{\pi}_0^i$ and $\boldsymbol{\pi}_1^i$ ($i = 1, ..., n_s$).

The solutions of the mentioned micromechanical problems allow to compute the displacements jumps in the j-th subset $\mathscr{S}^j$ in this form:

$$\mathbf{s}_{\mathbf{E}}^j = \mathbf{R}^j \mathbf{E} \qquad \mathbf{s}_{\boldsymbol{\pi}_0^i}^j = \mathbf{R}_{\boldsymbol{\pi}_0^i}^j \boldsymbol{\pi}_0^i \qquad \mathbf{s}_{\boldsymbol{\pi}_1^i}^j = \mathbf{R}_{\boldsymbol{\pi}_1^i}^j \boldsymbol{\pi}_1^i \tag{8}$$

where $\mathbf{R}^j(x_{T1}^j, x_{T2}^j)$, $\mathbf{R}_{\boldsymbol{\pi}_0^i}^j(x_{T1}^j, x_{T2}^j)$ and $\mathbf{R}_{\boldsymbol{\pi}_1^i}^j(x_{T1}^j, x_{T2}^j)$ denote the localization matrices of the displacement jumps $\mathbf{s}_{\mathbf{E}}^j(x_{T1}^j, x_{T2}^j)$, $\mathbf{s}_{\boldsymbol{\pi}_0^i}^j(x_{T1}^j, x_{T2}^j)$ and $\mathbf{s}_{\boldsymbol{\pi}_1^i}^j(x_{T1}^j, x_{T2}^j)$, obtained by alternatively applying $\mathbf{E}$, $\boldsymbol{\pi}_0^i$ and $\boldsymbol{\pi}_1^i$, respectively. In detail, the k-th column of $\mathbf{R}^j(x_{T1}^j, x_{T2}^j)$ lists the displacement jumps arising at the generic point of the subset $\mathscr{S}^j$ when only the k-th component of $\mathbf{E}$ is prescribed on the UC. The columns of $\mathbf{R}_{\boldsymbol{\pi}_0^i}^j(x_{T1}^j, x_{T2}^j)$ and $\mathbf{R}_{\boldsymbol{\pi}_1^i}^j(x_{T1}^j, x_{T2}^j)$ are evaluated in the same way, but assuming $\boldsymbol{\pi}_0^i$ and $\boldsymbol{\pi}_1^i$ as input actions. Then, the other required operators are computed using the localization matrices in Eq. (8). These are defined as:

$$\tilde{\tilde{\mathbf{R}}}^j = \left[\overline{\mathbf{R}}^{jT} \ \tilde{\mathbf{R}}^{jT}\right]^T \qquad \tilde{\tilde{\mathbf{R}}}_{\boldsymbol{\pi}_0^i}^j = \left[\overline{\mathbf{R}}_{\boldsymbol{\pi}_0^i}^{j\ T} \ \tilde{\mathbf{R}}_{\boldsymbol{\pi}_0^i}^{jT}\right]^T \qquad \tilde{\tilde{\mathbf{R}}}_{\boldsymbol{\pi}_1^i}^j = \left[\overline{\mathbf{R}}_{\boldsymbol{\pi}_1^i}^{j\ T} \ \tilde{\mathbf{R}}_{\boldsymbol{\pi}_1^i}^{jT}\right]^T \tag{9}$$

7

where $\overline{\mathbf{R}}^j$, $\overline{\mathbf{R}}^j_{\boldsymbol{\pi}^i_0}$ and $\overline{\mathbf{R}}^j_{\boldsymbol{\pi}^i_1}$ are the average matrices evaluated over the j-th subset area on the basis of $\mathbf{R}^j(x^j_{T1}, x^j_{T2})$, $\mathbf{R}^j_{\boldsymbol{\pi}^i_0}(x^j_{T1}, x^j_{T2})$ and $\mathbf{R}^j_{\boldsymbol{\pi}^i_1}(x^j_{T1}, x^j_{T2})$, while the columns of $\tilde{\mathbf{R}}^j$, $\tilde{\mathbf{R}}^j_{\boldsymbol{\pi}^i_0}$ and $\tilde{\mathbf{R}}^j_{\boldsymbol{\pi}^i_1}$ list the values of the displacement jump component π_{T2} computed in m properly selected points of the j-th subset. Figure Fig. 3(a) shows the location of these points for the example case of $m = 6$. The points, represented with yellow square dots, are equally spaced along the subset central line starting from the boundaries. Hence, the displacement jump vector $\tilde{\tilde{\mathbf{s}}}^j$, containing the average displacement jumps in all spatial directions and the local jumps in the m points along the UC thickness direction, is obtained by superimposing the effects of the previous contributions, as:

$$\tilde{\tilde{\mathbf{s}}}^j = \tilde{\tilde{\mathbf{R}}}^j \mathbf{E} + \sum_{i=1}^{n_s} \tilde{\tilde{\mathbf{R}}}^j_{\boldsymbol{\pi}^i_0} \boldsymbol{\pi}^i_0 + \sum_{i=1}^{n_s} \tilde{\tilde{\mathbf{R}}}^j_{\boldsymbol{\pi}^i_1} \boldsymbol{\pi}^i_1 \tag{10}$$

In a similar fashion, the strain fields in the bricks result as:

$$\boldsymbol{\varepsilon}^b_{\mathbf{E}} = \mathbf{P}^b \mathbf{E} \qquad \boldsymbol{\varepsilon}^b_{\boldsymbol{\pi}^i_0} = \mathbf{P}^b_{\boldsymbol{\pi}^i_0} \boldsymbol{\pi}^i_0 \qquad \boldsymbol{\varepsilon}^b_{\boldsymbol{\pi}^i_1} = \mathbf{P}^b_{\boldsymbol{\pi}^i_1} \boldsymbol{\pi}^i_1 \tag{11}$$

being $\mathbf{P}^b(x_1, x_2, x_3)$, $\mathbf{P}^b_{\boldsymbol{\pi}^i_0}(x_1, x_2, x_3)$ and $\mathbf{P}^b_{\boldsymbol{\pi}^i_1}(x_1, x_2, x_3)$ the localization matrices able to recover local strain values at any point of the bricks, given $\mathbf{E}$, $\boldsymbol{\pi}^i_0$ and $\boldsymbol{\pi}^i_1$.

Finally, the shell generalized stresses $\boldsymbol{\Sigma}$ are computed by invoking the generalized Hill-Mandel principle [2, 3], which leads to:

$$\boldsymbol{\Sigma} = \frac{1}{A} \int_A \int_{-t/2}^{t/2} \mathbf{B}^T \boldsymbol{\sigma}^b \, dx_3 \, dA \tag{12}$$

being $A = 2a_1 \times 2a_2$ the area of the UC-mid plane (see Fig. 2(a)). Hence, by accounting for the brick constitutive law and introducing Eq. (11), it results:

$$\begin{aligned}
\boldsymbol{\Sigma} &= \frac{1}{A} \int_A \int_{-t/2}^{t/2} \mathbf{B}^T \mathbf{C}^b \left[\mathbf{P}^b \mathbf{E} + \sum_{i=1}^{n_s} \mathbf{P}^b_{\boldsymbol{\pi}^i_0} \boldsymbol{\pi}^i_0 + \sum_{i=1}^{n_s} \mathbf{P}^b_{\boldsymbol{\pi}^i_1} \boldsymbol{\pi}^i_1 \right] dx_3 \, dA = \\
&= \overline{\mathbf{C}} \mathbf{E} + \sum_{i=1}^{n_s} \overline{\mathbf{C}}_{\boldsymbol{\pi}^i_0} \boldsymbol{\pi}^i_0 + \sum_{i=1}^{n_s} \overline{\mathbf{C}}_{\boldsymbol{\pi}^i_1} \boldsymbol{\pi}^i_1
\end{aligned} \tag{13}$$

4.2. Online phase

Matrices $\overline{\mathbf{C}}$, $\overline{\mathbf{C}}_{\boldsymbol{\pi}^i_0}$, $\overline{\mathbf{C}}_{\boldsymbol{\pi}^i_1}$, $\tilde{\tilde{\mathbf{R}}}^j$, $\tilde{\tilde{\mathbf{R}}}^j_{\boldsymbol{\pi}^i_0}$, $\tilde{\tilde{\mathbf{R}}}^j_{\boldsymbol{\pi}^i_1}$ ($i = 1, ..., n_s$, $j = 1, ..., n_s$) are used to solve the evolutionary nonlinear problem of the UC within the multiscale analysis. In the spirit of the displacement-based FE method, at the current global Newton–Raphson iteration, the strain vector $\mathbf{E}$ is given at each point of the structural model, whereas the stress vector $\boldsymbol{\Sigma}$ has to be determined through Eq. (13) on the basis of the updated values of the inelastic vectors $\boldsymbol{\pi}^i_0$ and $\boldsymbol{\pi}^i_1$ ($i = 1, ..., n_s$). To determine these latter, the evolution problem of the damage and friction variables in each subset is solved by means of an iterative elastic predictor-inelastic corrector procedure, as summarized in the following.

First, the displacement jumps are evaluated in each subset by using Eq. (10) and assuming the inelastic vectors as frozen at the previous step. On the basis of these quantities, the damage and unilateral-contact friction problems are solved in each subset by using the evolution law reported in Section 3. In particular, the average displacement

8

jump values recovered by means matrices $\overline{\mathbf{R}}^j, \overline{\mathbf{R}}^j_{\boldsymbol{\pi}_0^i}, \overline{\mathbf{R}}^j_{\boldsymbol{\pi}_1^i}$ are used to compute the inelastic vectors $\boldsymbol{\pi}_0^j$, whereas the displacement jumps derived from $\tilde{\mathbf{R}}^j, \tilde{\mathbf{R}}^j_{\boldsymbol{\pi}_0^i}, \tilde{\mathbf{R}}^j_{\boldsymbol{\pi}_1^i}$ are employed to evaluate $\boldsymbol{\pi}_1^j$. In fact, the local values of the displacement jump component π_{T2} along the UC thickness direction, combined with the average values in the other two directions, allow to solve the damage-friction problems in the chosen m points of the analyzed subset and, then, to compute $\boldsymbol{\pi}_1^j$ by solving the following problem of minimum:

$$\min_{\boldsymbol{\pi}_1^j} \left\{ \sum_{h=1}^m \left[\boldsymbol{\pi}_0^j + x_s^{j,h} \boldsymbol{\pi}_1^j - \boldsymbol{\pi}^j \left(x_s^{j,h} \right) \right]^2 \right\} \tag{14}$$

where $x_s^{j,h}$ is the coordinate of m-th point, with $h = 1, ..., m$. To be noted is that, for the special NUTFA proposed, the problem of minimum in Eq. (14) is actually solved referring only to the inelastic component directed along x_{T2}. Once $\boldsymbol{\pi}_0^j$ and $\boldsymbol{\pi}_1^j$ ($j = 1, ..., n_s$) are updated, a further iteration is performed by solving again the damage, unilateral contact and sliding friction problems in all subsets. The procedure continues until convergence for the values of $\boldsymbol{\pi}_0^i$ and $\boldsymbol{\pi}_1^i$ ($i = 1, ..., n_s$) is reached. Finally, the stress vector $\boldsymbol{\Sigma}$ is computed according to Eq. (13), thus providing the constitutive response of the shell at the macroscale.

5. Single UC response

To investigate the performance of the presented model at the material level, the response of a running bond masonry UC is studied under two typical loading histories (LHs) involving the out-of-plane behavior. Brick size and mortar joint thickness are set equal to $240 \times 60 \times 120\,\text{mm}^3$ and $10\,\text{mm}$, respectively. Mechanical properties of both of them are contained in the first row of Table 1, being E_b and G_b the Young's and shear moduli of the bricks used to construct the isotropic elastic stiffness matrix $\mathbf{C}^b$.

Table 1: Material parameters for bricks and mortar used for the UC and the masonry elements analyzed in Sections 5 and 6 .

E_b [MPa]	G_b [MPa]	C_N $\left[\text{N/mm}^3\right]$	C_T $\left[\text{N/mm}^3\right]$	t_N^0 [MPa]	t_T^0 [MPa]	G_{cN} [N/mm]	G_{cT} [N/mm]	μ [-]
18000	7826.1	100	43.5	0.50	0.44	1.25×10^{-2}	2.17×10^{-2}	0.50
52700	22913.1	100	43.5	0.15	0.15	3.00×10^{-3}	3.00×10^{-3}	0.50
4000	1666.7	140	58.3	0.10	0.27	3.00×10^{-4}	4.00×10^{-1}	0.37
4260	1775.0	1000	1000	0.35	0.19	2.50×10^{-4}	1.25×10^{-1}	0.58

The first test (LH1) analyzes the UC behavior under curvature about x_2 axis combined with membrane tensile strain in x_1 direction. In detail, linearly increasing curvature K_{11} and tensile strain $E_{11} = t K_{11}$ are applied to the UC up to the final value $K_{11} = 4 \times 10^{-6}\,\text{mm}^{-1}$. Similarly, the second test (LH2) considers linearly increasing curvature K_{12} and tensile strains $E_{11} = E_{22} = \frac{t}{4} K_{12}$ up to the final value $K_{12} = 1.5 \times 10^{-5}\,\text{mm}^{-1}$. In [2], the UC response

9

was analyzed under the same loading conditions with the uniform TFA approach, obtaining inaccurate results with coarse 'in-plane' subset discretizations, i.e. assuming $n_h = 1$ and $n_b = 2$. Thus, the effects of both denser subset partitions and the assumption of non-uniform distributions of inelastic quantities in each subdomain are investigated in this study. In detail, four alternative subset discretizations are considered in the numerical simulations. These all divide the UC into $n_t = 8$ layers across the thickness $t = 120\,\text{mm}$, but assume different subset arrangements in the in-plane directions, as depicted in Figs. 4(a)-4(d). Model (a), indicated as TFA 1 + 2, considers $n_h = 1$ and $n_b = 2$ subsets for the head and bed joints, respectively, in each layer, based on the uniform TFA approach; similarly, models (b) and (c), TFA 2 + 6 and TFA 4 + 10, consider $n_h = 2$ with $n_b = 6$ and $n_h = 4$ with $n_b = 10$ subsets for the head and bed joints based on uniform TFA, respectively; finally, model (d), NUTFA 1 + 2, considers $n_h = 1$ and $n_b = 2$ subsets for the head and bed joints, respectively, but based on the linear NUTFA approach. For the latter, $m = 6$ points are used in each subset (yellow square dots) to evaluated the linear variation $x_s^i \boldsymbol{\pi}_1^i$ of the inelastic displacement jumps in Eq. (7).

To solve the offline micromechanical problems (Section 4.1), FE analyses of the UC are performed adopting standard 8-node hexaedral isoparametric elements [36] to model the masonry bricks and 4+4-node plane isoparametric interface elements for the mortar joints. Of course, other higher order finite elements could be used or even other numerical approaches could be used.

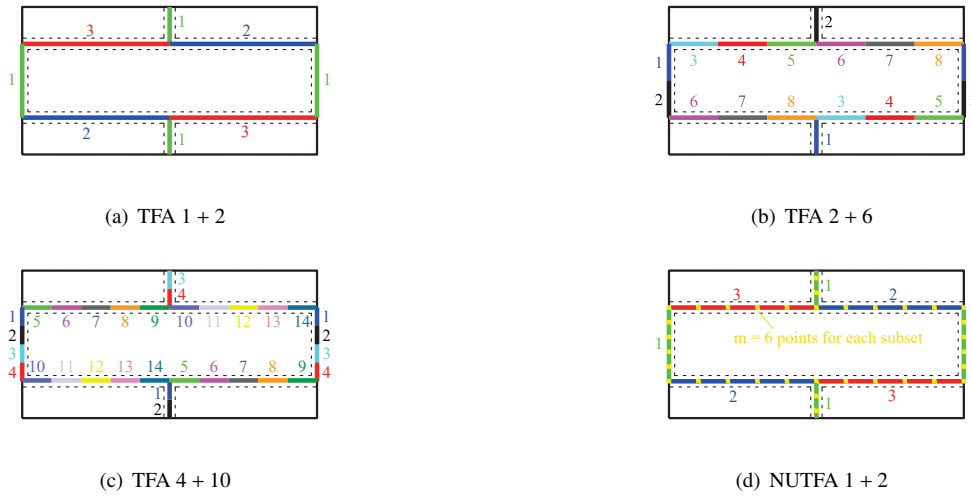(a) TFA 1 + 2

(b) TFA 2 + 6

(c) TFA 4 + 10

(d) NUTFA 1 + 2

Figure 4: Subset subdivision in each layer of the UC (colors and numbers indicate the region of the UC belonging to the same subset)

Fig. 5(a) contains the UC response to LH1 in terms of average bending moment M_{11} versus average curvature K_{11} for all models. It appears that, when the number of 'in-plane' subsets increases, the uniform TFA prediction (blue, violet and red curves) converges to the reference solution obtained with a detailed FE micromechanical model (black curve) based on the same constitutive assumptions. The best result is obtained with NUTFA 1 + 2, as this model accurately capture the distribution of the inelastic quantities over mortar joints. This is evident from Fig. 6, where
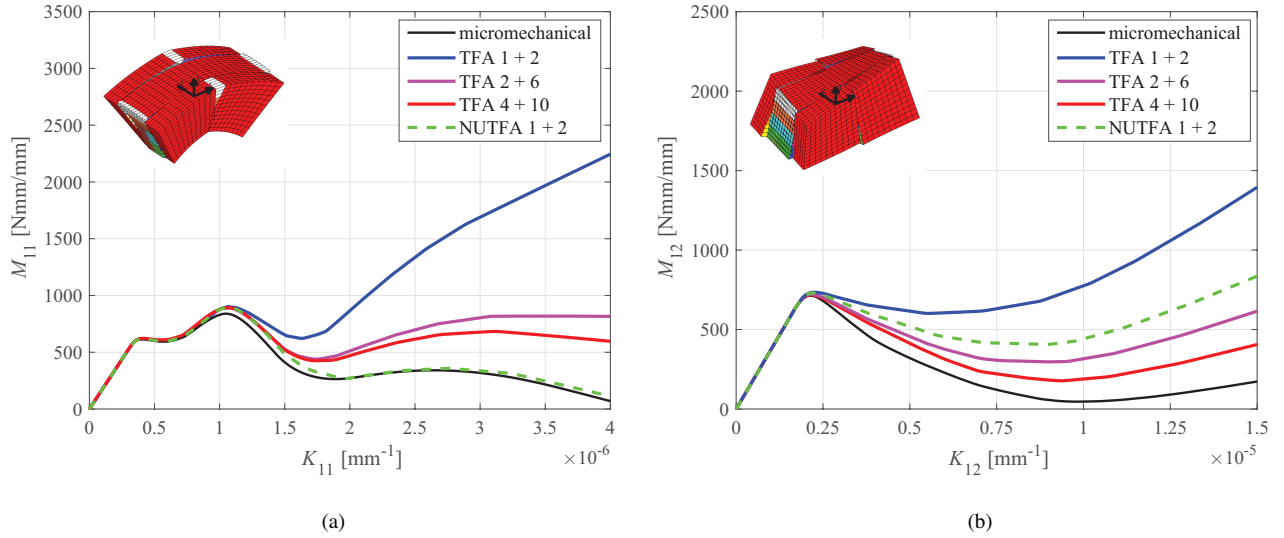
10

Figure 5: Response of the UC to (a) LH1 and (b) LH2 in terms of average moments M_{11}, M_{12} versus average curvatures K_{11}, K_{12}

the variation of the component π_{T2} along the bed joint subsets extracted from the first layer of the UC is plotted for both micromechanical (black curves) and NUTFA (green curves) models. Note that, for this loading conditions, π_{T2} is equal to zero in the head joints. At the beginning of the loading histories, i.e. at $K_{11} = 1.1 \times 10^{-6}$ mm (Fig. 6(a)), nonlinear variation of π_{T2} is detected with the micromechanical model. Thus, the NUTFA model also approximately describes the occurring nonlinear field at this stage. However, as the analysis goes on, a fairly linear trend appears for π_{T2} in the micromechanical simulation (Fig. 6(b)), in accordance with the prescribed variation of the inelastic displacement jumps in the NUTFA model (see Eq. (7) and Fig. 3(b)), thus leading to a perfect match of the global curves in Fig. 5(a).

Finally, the curves in Fig. 5(b) show the UC response to LH2 in terms of average torsional moment M_{12} versus average curvature K_{12}. For this loading history, the proposed NUTFA 1 + 2 procedure significantly improves the results obtained with the uniform TFA 1 + 2, but, differently from the previous case, the micromechanical results are not accurately reproduced. In fact, in this case, the best solution is achieved with the uniform TFA 4 + 10 that better describes the inelastic displacement field in the UC.

6. Masonry structural element response

To study the performance of the proposed model in reproducing the response of real masonry structures, three significant examples are presented in the following.

The multiscale simulations are based on the use, at the macroscale, of a 4-node shell FE obtained by coupling a standard 4-node isoparametric membrane FE with a 4-node MITC plate model [7]. Hence, bi-linear shape fuctions are used for the membrane problem to interpolate V_1 and V_2, while the plate problem is addressed by interpolating
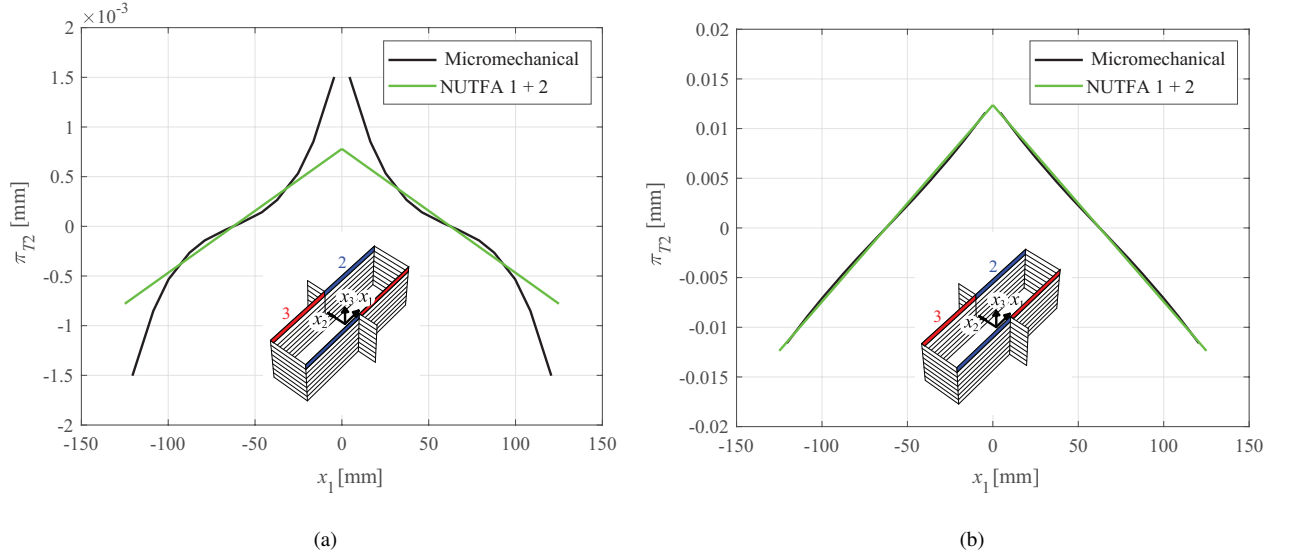
11

Figure 6: Distribution of the inelastic component π_{T2} in the bed joint subsets extracted from the first layer identified along the UC thickness: results for LH1 at a) $K_{11} = 1.1 \times 10^{-6} \text{mm}^{-1}$ and b) $K_{11} = 2.3 \times 10^{-6} \text{mm}^{-1}$

Γ_{13} and Γ_{23} independently on V_3, Φ_1 and Φ_2, according to the model proposed in [8]. As drill degrees of freedom are not directly included in the shell formulation, to manage possible singularities of the global structure stiffness matrix, the standard approach described in [7] is used, which consists in introducing proper defined rotational springs at the mesh nodes.

As for the regularization technique required in presence of strain-softening behavior the proposed model is suitable for the use of different strategies. Hence, in the numerical tests presented the nonlocal integral and fracture energy-based approach are alternatively employed at the macroscale.

To solve the offline micromechanical problems (Section 4.1), the same FE approach used for the single UC response is adopted.

6.1. Vertically loaded masonry slab

The behavior of a simply supported masonry slab vertically loaded at the mid-span is analyzed. The specimen is characterized by a running bond texture obtained by arranging $230 \text{ mm} \times 76 \text{ mm} \times 110 \text{ mm}$ bricks with 10 mm thick mortar. Overall size and loading conditions considered are depicted in Fig. 7. Similar specimen was studied in [28]. Second row of Table 1 is referenced for the mechanical parameters assumed for the constituent materials.

To assess effectiveness of the presented formulation, the results obtained with the multiscale model are compared with those evaluated through a detailed micromechanical model, based on the same constitutive assumptions. The latter model discretizes bricks and mortar joints with solid linear-elastic 8-node hexaedral isoparametric elements and 4+4-node nonlinear isoparametric interface elements, respectively [3].

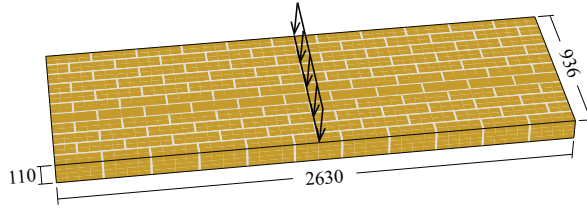Fig. 8 compares the load-deflection curves obtained with the proposed multiscale approach with that deriving

12

Figure 7: Geometry of the masonry slab vertically loaded (dimensions in millimeters)

from the micromechanical simulation (black curve). The multiscale analyses are based on different in-plane subset arrangements, all dividing the UC thickness in $n_t = 10$. The blue curve refers to the case of uniform TFA $1 + 2$, the red curve to the uniform TFA $1 + 10$ and the green curve to the NUTFA $1 + 2$. The nonlocal integral approach is adopted to regularize the numerical solutions [3], by adopting a nonlocal radius equal to 35 cm.

The results clearly show that the TFA $1 + 2$ model leads to a wrong evaluation of the structural performance, as this model considers piece-wise uniform distributions of inelastic quantities and coarse in-plane subset discretization. By contrast, good predictions are detected with the uniform TFA $1 + 10$ and NUTFA $1 + 2$ models. The peak loads and softening branches satisfactorily reproduce the micromechical behavior. However, the total number of inelastic variables to be determined in the NUTFA $1 + 2$ model is lower than that required from TFA $1 + 10$, and, thus, the NUTFA $1 + 2$ is computationally less expensive than the TFA $1 + 10$.

According to the micromechanical results, damage firstly develops in the head joint subsets located at the mid-span due to mode I of fracture and, then, spreads around affecting also the bed joint subsets. Fig. 9 shows the resulting damage distribution, plotted in the amplified deformed configuration of the structure, referred to (a) micromechanical and (b) multiscale NUTFA $1 + 2$ models, respectively.
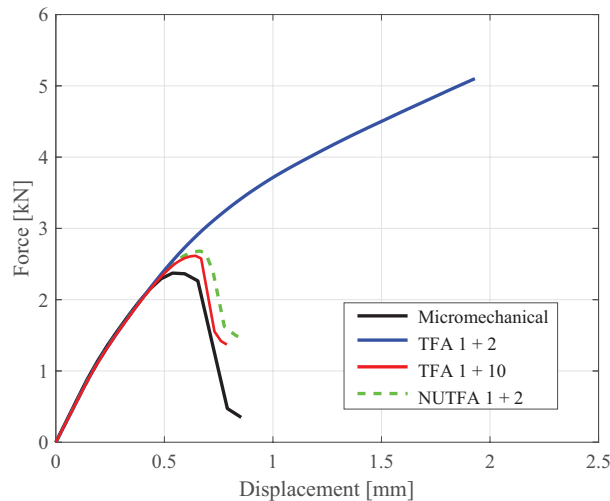

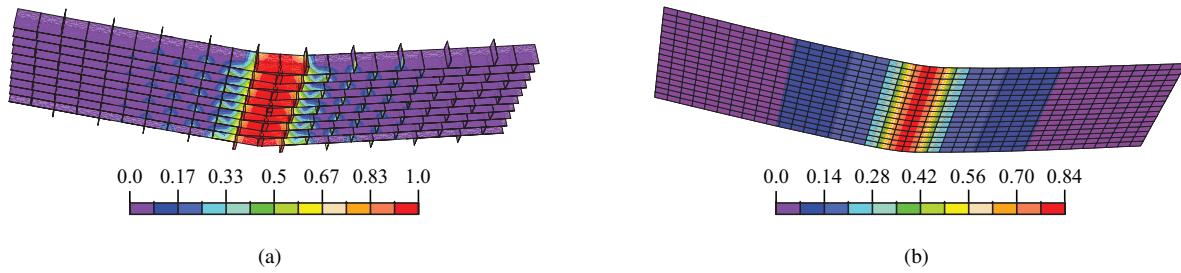Figure 8: Global response curves of the masonry slab in Fig. 7

13

Figure 9: Crack pattern at the end of the analyses: (a) distribution of the damage variable D at the interfaces for the micromechanical model and (b) average damage occurring in the UC subsets of the multiscale NUTFA 1 + 2 model

6.2. Masonry wall under eccentric load

The second application concerns the unreinforced wall depicted in Fig. 10. This specimen was experimentally tested during the campaign conducted by D'Ambra et al. [13] and its structural behavior is numerically studied in [12, 32]. The geometry of the wall considers a running bond arrangement for the $250 \times 55 \times 120\,\mathrm{mm}^3$ clay bricks, with mortar joints having an average thickness of $10\,\mathrm{mm}$.

A UPN steel beam is placed at the base to connect the wall to the floor, so that a cylindrical hinge boundary restraint configuration is obtained at the bottom edge. A second UPN steel beam is placed on one lateral edge. This is fixed to a rigid steel frame in order to provide a fully clamped restraint configuration on this edge. Hence, a concentrated load, orthogonal to the wall plane, is applied at the top corner on the opposite vertical edge, to induce a double-bending stress state. The load is applied by means of an hydraulic jack and a $300\,\mathrm{mm} \times 300\,\mathrm{mm} \times 10\,\mathrm{mm}$ steel plate, and is constantly increased under displacement control until specimen failure.
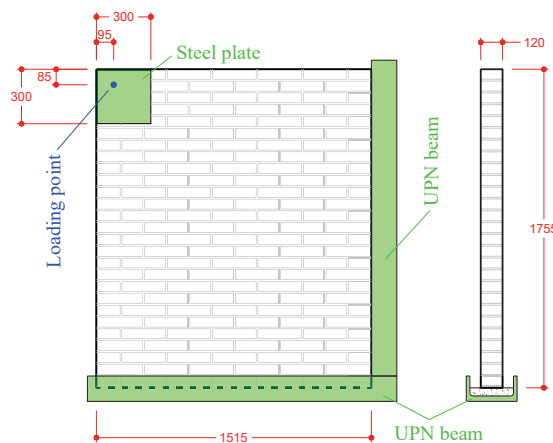

Figure 10: Geometry of the masonry wall subjected to out-of-plane loading (dimensions in millimeters)

The mechanical behavior of the wall is numerically reproduced by the proposed multiscale shell model, adopting the material parameters calibrated in [12] for the bricks and mortar, and reported in the third row of Table 1.

14

The FE mesh for the masonry consists of $20 \times 21 = 420$ rectangular elements, while the loading steel plate is explicitly modeled with additional linear elastic shell FEs. The edge UPN beams are simulated by imposing proper boundary conditions to the wall. In particular, for nodes located at the bottom edge, all three displacement components are restrained, while rotations are permitted. By contrast, although the vertical beam was fixed to a rigid frame, it emerged that this was not able to provide full rotational restraint about its axis. Therefore, for nodes located at the fixed lateral edge, all displacement and rotation components are restricted except for the rotation about the vertical direction. To simulate the partial flexibility of the beam, distributed rotational springs are applied along the vertical direction.

Three alternative subset discretizations are considered in the numerical simulations. These all consider the UC thickness divided in $n_t = 10$, but assume different subset arrangements in the in-plane directions, as depicted in Figs. 4(a), 4(c) and 4(d). Hence, in the following, the results obtained with the uniform TFA $1 + 2$ and $4 + 10$ are compared with those evaluated with NUTFA $1 + 2$.

Fig. 11 shows the global response curves obtained with the proposed multiscale model in terms of applied force versus out-of-plane displacement of the loaded point. These are compared to the experimental results (black curve). All numerical models give the same solution until the applied load reaches the value of about 2.3 kN, i.e. when a diagonal crack starts growing from the top corner of the fixed vertical edge to mid-height of the opposite edge (see also Fig. 12(b)), due to the bending deformations of the wall that couple with the torsional one. For higher load, TFA $4 + 10$ (red curve), which considers a piece-wise uniform but detailed approximation of the mortar inelastic deformations, gives good results, correctly capturing wall collapse. By contrast, TFA $1 + 2$ (blue curve), with a coarse piece-wise uniform subset discretization, cannot reproduce the failure mechanism, although it shows the correct crack formation pattern. Finally, NUTFA $1 + 2$, with a coarse but piece-wise linear inelastic deformation assumption, almost well matches the TFA $4 + 10$ solution and the experimental outcomes. For this model, Fig. 12 shows (a) the distribution of the average damage occurring in all subsets of the UC and compares it with (b) the experimental counterpart.

6.3. Masonry vault under differential settlements

The proposed multiscale NUTFA model is used to analyze the response of a masonry barrel vault under differential settlements. The specimen, schematically shown in Figure 13, is characterized by the following overall geometric parameters: medium radius equal to 2060 mm, span and width equal to 3980 mm. The running bond texture is obtained by arranging $250 \times 55 \times 120$ mm³ bricks and mortar joints with average thickness equal to 10 mm, resulting in a vault thickness equal to 120 mm.

The structural behavior is studied under a horizontal displacement along the Z direction imposed at one of the abutments (Fig. 13). A two-step analysis is performed: first, the self weight is applied; then, the imposed displacement is gradually increased up to its final value of 5 mm. Mechanical parameters ruling the response of bricks and interfaces are contained in the last row of Table 1. These are set according to data reported in [1], where same specimen is tested by adopting a micromechanical model made up of 3D solid FEs for the bricks and plane interfaces for the mortar joints.
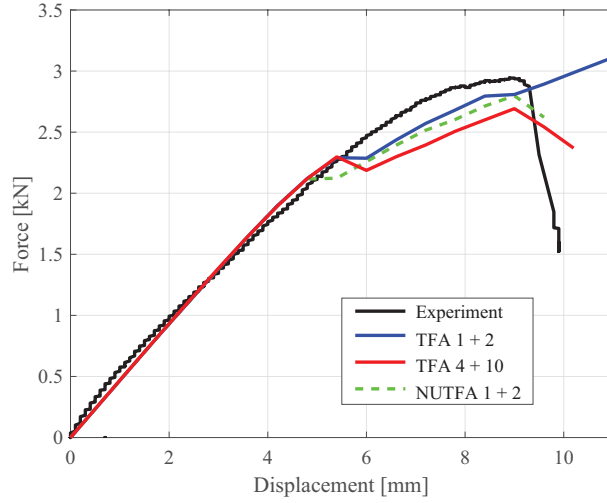
15

Figure 11: Global response curves of the wall under out-of-plane load

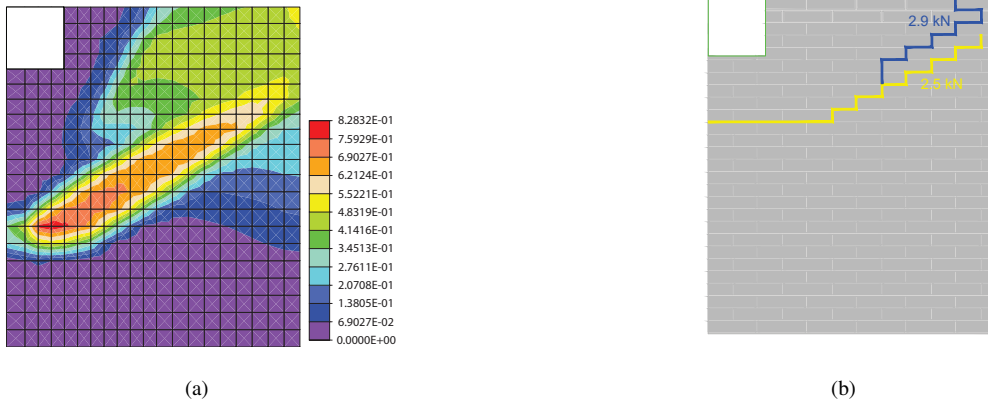(a)   (b)

Figure 12: Crack pattern: (a) average damage distribution obtained with the NUTFA 1 + 2 model at the out-of-plane displacement of the loaded point equal to 7.2 mm and (b) experimental outcomes [12, 13]

Hence, the numerical outcomes obtained with the presented multiscale formulation are compared in the following with those derived from the detailed model adopted in [1].

The NUTFA simulation is performed subdividing the representative UC in $n_t = 10$ layers across the thickness and assuming $n_b = 2$ and $n_h = 1$, similarly to Figure 4(d). The resulting load-displacement global curves obtained with the two models are shown in Figure 14, exhibiting an overall good match. The discrepancies shown in the figure are a consequence of the different intrinsic characteristic of the two models. In fact, as opposed to the continuum shell model here proposed, the model in [1] explicitly considers the heterogeneous and discrete nature of masonry.

Moreover, the multiscale solution (green dashed curve) shows an irregular trend and a slightly more flexible response with respect to the referred micromechanical curve. Each drop in the resisting force is due to the sudden formation of a damaged area that involves a large portion of the vault, comparable to the single FE size, while, in a

16

real specimen, damage is confined to the size of mortar joint. Thus, the effect of the damaging process is a little more evident than in the micromechanical solution.

Figure 15 shows the distribution of the average damage in the subsets of the UC. This is plotted over the (amplified) deformed configuration of the vault at the last step of the analysis. In agreement with the failure mode predicted in [1], four significant cracks arise along mortar joints. In particular, damage starts at the vault abutments and, then, propagates towards the middle of the vault forming two diagonal bands.
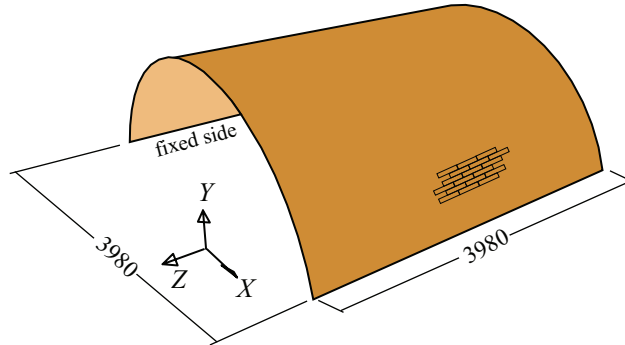

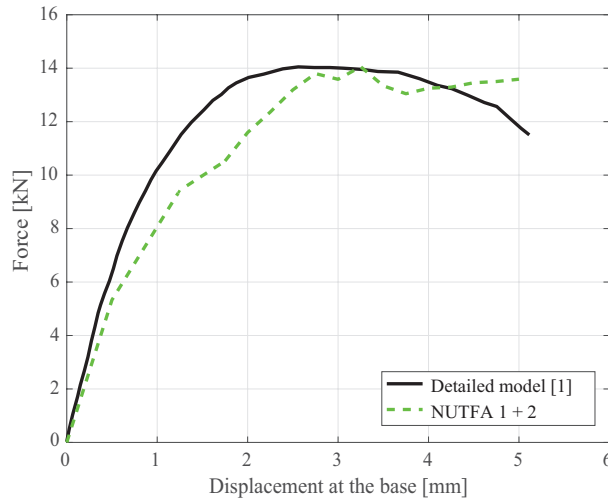Figure 13: Schematic of the analyzed masonry vault (dimension in millimeters)

Figure 14: Global response curves of the vault under differential settlements

7. Conclusions

In this work an enhanced Transformation Field Analysis procedure tailored to the multiscale analysis of periodic masonry has been presented. The response of the shell model at the macroscale is deduced via homogenization from that of a representative 3D unit cell defined at the microscale. The nonlinear parts of the UC, i.e. the interfaces representing mortar joints, are divided into regions where pre-assumed non-uniform variations of the inelastic quantities
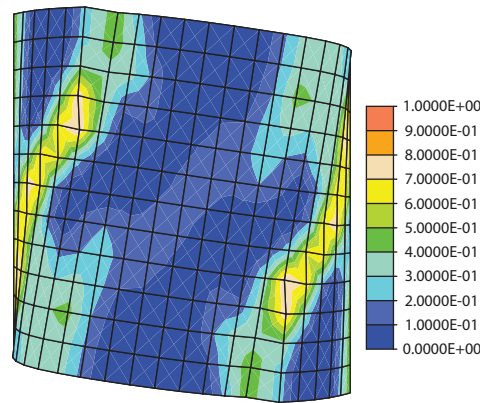
17

Figure 15: Average damage distribution at the ultimate imposed displacement obtained with the NUTFA 1 + 2 model

are considered. In detail, linear interpolation along the UC mid-plane is adopted for the inelastic component directed along the UC thickness, accounting for damage and slip. This assumption permits to avoid the fine subset partitions needed in case of piece-wise uniform distributions of nonlinearities over mortar joints [2, 3], but requires to solve the damage and friction problems in further points identified in each subset.

Effectiveness of the proposed NUTFA model has been proved at both material and structural level by analyzing the bending and torsional behavior of a running bond UC and the response of three masonry structures, respectively. The numerical results have been compared to micromechanical and experimental outcomes, considered as reference solutions, and a comparative study has been conducted to evaluate advantages and disadvantages of the adoption of the NUTFA with respect to the uniform TFA.

The numerical simulations of the UC showed that the NUTFA model impressively improves predictions of the uniform TFA model, if the same coarse subset 'in-plane' partition is considered for the two models. Instead, in case of torsional behavior, the NUTFA solution poorly approaches the micromechanical one and, thus, in this case, the best evaluation of the micromechanical behavior is achieved with the uniform TFA characterized by refined subset arrangement. At the structural level, the NUTFA model satisfactorily describes the overall response of the analyzed elements, proving to be able to predict failure load and occurring cracking paths.

To summarize, the proposed NUTFA appears as an effective alternative tool to the uniform TFA to analyze the response of regular masonry, also considering curved geometry and subjected to both in-plane and out-of-plane loading conditions. Certainly, the technique can be further improved by including higher order variations of the nonlinear variables over each subdomain, such as parabolic or cubic, but this in turn increases the model complexity making harder the solution of the damage-friction problem in each subset.

References

[1] P. Adam, P. Bartolomeo, C. Corrado, M. Lorenzo, B.A. Izzuddin, B. Ingrid, N. Gattesco, Nonlinear simulation of masonry vaults under earthquake loading, in: Proceedings 8th International Conference on Computational Methods in Structural Dynamics and Earthquake Engineering,

volume 1, pp. 595–606.

[2] D. Addessi, P. Di Re, C. Gatta, E. Sacco, Multiscale analysis of out-of-plane masonry elements using different structural models at macro and microscale, Computers & Structures 247 (2021) 106477.

[3] D. Addessi, P. Di Re, C. Gatta, E. Sacco, Shell-3D multiscale modeling of masonry vaults based on the TFA procedure, International Journal for Multiscale Computational Engineering 20 (2022) 13–42.

[4] D. Addessi, C. Gatta, S. Marfia, E. Sacco, Multiscale analysis of in-plane masonry walls accounting for degradation and frictional effects, International Journal for Multiscale Computational Engineering 18 (2020) 159–80.

[5] D. Addessi, S. Marfia, E. Sacco, J. Toti, Modeling approaches for masonry structures, The Open Civil Engineering Journal 8 (2014) 288–300.

[6] A. Amendola, A. Fortunato, F. Fraternali, O. Mattei, G. Milton, P. Seppecher, Limit analysis of strut nets, Mathematics and Mechanics of Solids (2022).

[7] K. Bathe, Finite element procedures, Prentice Hall, Pearson Education Inc., 2006.

[8] K. Bathe, E. Dvorkin, A four-node plate bending element based on Mindlin/Reissner plate theory and a mixed interpolation, International Journal for Numerical Methods in Engineering 21 (1985) 367–83.

[9] D. Briccola, M. Bruggi, Analysis of 3D linear elastic masonry-like structures through the API of a finite element software, Advances in Engineering Software 133 (2019) 60–75.

[10] A. Castellano, A. Fraddosio, D. Oliveira, M. Piccioni, E. Ricci, E. Sacco, An effective numerical modelling strategy for FRCM strengthened curved masonry structures, Engineering Structures 274 (2023) 115116.

[11] A.M. D'Altri, V. Sarhosis, G. Milani, J. Rots, S. Cattari, S. Lagomarsino, E. Sacco, A. Tralli, G. Castellazzi, S. de Miranda, Modeling strategies for the computational analysis of unreinforced masonry structures: review and classification, Archives of Computational Methods in Engineering 27 (2020) 1153–85.

[12] C. D'Ambra, G. Lignola, A. Prota, F. Fabbrocino, E. Sacco, FRCM strengthening of clay brick walls for out of plane loads, Composites Part B: Engineering 174 (2019) 107050.

[13] C. D'Ambra, G. Lignola, A. Prota, E. Sacco, F. Fabbrocino, Experimental performance of FRCM retrofit on out-of-plane behaviour of clay brick walls, Composites Part B: Engineering 148 (2018) 198–206.

[14] M. De Piano, M. Modano, G. Benzoni, V. Berardi, F. Fraternali, A numerical approach to the mechanical modeling of masonry vaults under seismic loading, Ingegneria Sismica 34 (2017) 104–20.

[15] P. Di Re, D. Addessi, E. Sacco, A multiscale force-based curved beam element for masonry arches, Computers & Structures 208 (2018) 17–31.

[16] G. Dvorak, Transformation field analysis of inelastic composite materials, Proceedings of the Royal Society of London A 437 (1992) 311–27.

[17] F. Fritzen, T. Bohlke, Three-dimensional finite element implementation of the nonuniform transformation field analysis, International Journal for Numerical Methods in Engineering 84 (2010) 803–29.

[18] N. Grillanda, A. Chiozzi, G. Milani, A. Tralli, Collapse behavior of masonry domes under seismic loads: an adaptive NURBS kinematic limit analysis approach, Engineering Structures 200 (2019) 109517.

[19] N. Grillanda, M. Valente, G. Milani, A. Chiozzi, A. Tralli, Advanced numerical strategies for seismic assessment of historical masonry aggregates, Engineering Structures 212 (2020) 110441.

[20] P. Lourenço, Computations on historic masonry structures, Progress in Structural Engineering and Materials 4 (2002) 301–19.

[21] P. Lourenço, A. Gaetani, Finite element analysis for building assessment: advanced use and practical recommendations, Taylor & Francis, 2022.

[22] T.J. Massart, R.H.J. Peerlings, M. Geers, An enhanced multi-scale approach for masonry wall computations with localization of damage, International Journal for Numerical Methods in Engineering 69 (2007) 1022–59.

[23] J. Michel, P. Suquet, Nonuniform transformation field analysis, International Journal for Solids and Structures 40 (2003) 6937–55.

[24] B. Nela, A.J. Rios, M. Pingaro, E. Reccia, P. Trovalusci, Limit analysis of locally reinforced masonry arches, Engineering Structures 271 (2022) 114921.

[25] N. Nodargi, P. Bisegna, A new computational framework for the minimum thrust analysis of axisymmetric masonry domes, Engineering Structures 234 (2021) 111962.

[26] B. Pantò, L. Macorini, B. Izzuddin, A two-level macroscale continuum description with embedded discontinuities for nonlinear analysis of brick/block masonry, Computational Mechanics 69 (2022) 865–90.

[27] M. Petracca, L. Pelà, R. Rossi, S. Oller, G. Camata, E. Spacone, Multiscale computational first order homogenization of thick shells for the analysis of out-of-plane loaded masonry walls, Computer Methods in Applied Mechanics and Engineering 315 (2017) 273–301.

[28] M. Petracca, L. Pelà, R. Rossi, S. Oller, G. Camata, E. Spacone, Multiscale computational first order homogenization of thick shells for the analysis of out-of-plane loaded masonry walls, Computer Methods in Applied Mechanics and Engineering 315 (2017) 273–301.

[29] K. Raju, T. Tay, V. Tan, A review of the FE2 method for composites, Multiscale and Multidisciplinary Modeling, Experiments and Design 4 (2021) 1–24.

[30] P. Roca, M. Cervera, G. Gariup, L. Pelà, Structural analysis of masonry historical constructions. Classical and advanced approaches, Archives of Computational Methods in Engineering 17 (2010) 299–325.

[31] V. Sarhosis, J. Lemos, A detailed micro-modelling approach for the structural analysis of masonry assemblages, Computers & Structures 206 (2018) 66–81.

[32] J. Scacco, B. Ghiassi, G. Milani, P. Lourenço, A fast modeling approach for numerical analysis of unreinforced and FRCM reinforced masonry walls under out-of-plane loading, Composites Part B: Engineering 180 (2020) 107553.

[33] V. Sepe, S. Marfia, E. Sacco, A nonuniform TFA homogenization technique based on piecewise interpolation functions of the inelastic field, International Journal of Solids and Structures 50 (2013) 725–42.

[34] P. Trovalusci, D. Capecchi, G. Ruta, Genesis of the multiscale approach for materials with microstructure, Archive of Applied Mechanics 79 (2009) 981–97.

[35] C.V. Verhoosel, J.J.C. Remmers, M.A. Gutiérrez, R. de Borst, Computational homogenization for adhesive and cohesive failure in quasi-brittle solids, International Journal for Numerical Methods in Engineering 83 (2010) 1155–79.

[36] O. Zienkiewicz, R. Taylor, J. Zhu, The finite element method: its basis and fundamentals, Elsevier, 2005.